Title: Distinct C-tail dynamics between β-arrestin isoforms in forming GPCR tail- and core-engaged complexes

Authors: Ruibo Zhai[1,2,3,†], Jiening Wang[4,†], Xianhui Hou[2], Xiaogang Niu[2], Changwen Jin[2,3], Shan Wu[4,*], Yunfei Hu[1,*]

Affiliations:

[1] State Key Laboratory of Magnetic Resonance Spectroscopy and Imaging, National Center for Magnetic Resonance in Wuhan, Innovation Academy for Precision Measurement Science and Technology, Chinese Academy of Sciences, Wuhan, 430071, China

[2] Beijing Nuclear Magnetic Resonance Center, College of Chemistry and Molecular Engineering & Beijing National Laboratory for Molecular Sciences, Peking University, Beijing 100871, China

[3] School of Life Sciences, Peking University, Beijing, 100871, China

[4] Hubei Collaborative Innovation Center for Green Transformation of Bio-Resources, Hubei Key Laboratory of Industrial Biotechnology, School of Life Sciences, Hubei University, Wuhan, Hubei 430062, China

[†] These authors contributed equally to this work.

* Corresponding authors: S.W., wushan91@hubu.edu.cn; Y.H., huyunfei@wipm.ac.cn

Abstract:

The two non-visual β-arrestins (βarrs) are essential scaffolding proteins involved in desensitization, internalization and signaling of G protein-coupled receptors (GPCRs), and they show functional divergence despite high structural similarity. By employing NMR, cryo-EM and computational methods, we herein report previously unanticipated differences between the two isoforms in the basal and both the receptor tail- and core-engaged states. The autoinhibitory C-tails of the two βarrs show distinct dynamics in the basal state, and only that of βarr2 robustly transits into an α-helix that docks at the central crest in the tail-engaged state. This difference is encoded in the amino acid sequences of the disordered regions flanking the chameleon motif. Moreover, core interaction releases βarr2 C-tail, and the core-engaged complex structures determined in lipid nanodiscs reveal a less tilted binding angle of βarr2 due to a shallower insertion of its C-edge loops into the membrane. Our findings provide a conceptual molecular framework for understanding the functional divergence between the βarr isoforms in regulating GPCR signaling.

Main text:

Introduction

G protein-coupled receptors (GPCRs) are the largest family of cell-surface receptors and are important targets for drug discovery (*1*). GPCR signaling occurs via coupling to heterotrimeric G proteins or arrestins. Activation of the arrestin signaling pathway is dependent on receptor phosphorylation by GPCR kinases (GRKs) in the disordered C-terminal tail or intracellular loops, resulting in formation of GPCR-arrestin complexes that may terminate G protein signaling, induce receptor internalization, or stimulate G protein-independent signaling events (*2, 3*). The current established paradigm for arrestin activation highlights a two-step process involving the formation of the 'tail-engaged' and 'core-engaged' complexes with GPCRs, each possessing its unique functional roles (*4, 5*).

Unlike the G proteins, which comprise a total of 16 members belonging to four subfamilies in human, arrestins comprise only four isoforms, among which only two are ubiquitously expressed in non-visual cells known as the β-arrestins (βarrs), namely β-arrestin-1 (βarr1) and β-arrestin-2 (βarr2). Despite their high sequence and structural similarity, accumulating evidences suggest that the two βarr isoforms can carry out distinct, sometimes antagonizing physiological functions (*6-9*). Yet, the underlying mechanism remains poorly understood. One major limitation of the current structural data is that the majority of the GPCR-βarr complex structures were obtained using the βarr1 isoform (*10-17*). Recent efforts in comparative studies of the two isoforms unraveled previously unanticipated structural heterogeneity and diversity in GPCR-β-arrestin interactions (*18-20*). However, structural differences underlying functional divergence between isoforms remain enigmatic. Since the tail- and core-engaged complexes both contribute to βarr-signaling and are involved in distinct functionalities, a systematic study of both conformational states is expected to provide more comprehensive insights into their functional differences.

To this end, we combined solution NMR, cryo-EM and computational methods to conduct a comparative study of the structural and dynamical differences between the two βarr isoforms in both the tail- and core-engaged complexes. The NMR data demonstrate that the chameleon sequence in the C-terminal tail (C-tail) of βarr2, but not that of βarr1, robustly undergoes a β-to-α transition in the tail-engaged state, and that the formed helix occupies the receptor core-

binding site. The cryo-EM structures of the core-engaged complexes with a modified β_2 adrenergic receptor (β_2AR) determined in lipid nanodiscs further uncover subtle differences between the two βarr isoforms in binding with the receptor TM core and the membrane. Our findings illuminate distinct dynamics in βarr C-tail that can modulate their conformational energy landscapes, offering unprecedented mechanistic insights into their functional divergence.

Results

^{19}F NMR reveals distinct C-tail dynamics in βarrs

In our previous work, we have utilized ^{19}F NMR spectroscopy to characterize the conformational dynamics of human βarr1 (*21*). Herein, we further adapted this approach to the study of βarr2, enabling direct comparison between the two isoforms. The amino acid sequences of human βarr1 and βarr2 show prominent differences in their C-tails (Fig. 1A, Fig. S1), a critical regulatory region that not only plays an autoinhibitory role but also contains binding sites for adaptin, clathrin and probably signaling kinases (*22-25*). Owing to intrinsic flexibility, most parts of the βarr C-tails remain unresolved in available structures. To obtain comprehensive information on the C-tail dynamics, we selected six sites in both βarr1 and βarr2 spanning the proximal, middle, and distal segments of the C-tail (Fig. 1A–C, Fig. S2), and mutated each of them to cysteine for ^{19}F probe labeling. ^{19}F NMR spectra were collected for both βarrs in the basal state and in complex with V2Rpp, a classical phosphopeptide derived from the V2 vasopressin receptor tail, revealing unanticipated differences in C-tail dynamics (Fig. 1D–H).

In the basal state, we observed significantly higher conformational heterogeneity in βarr2 C-tail. In particular, the βarr2 F388C site (designated as F388C$^{\beta arr2}$) in the middle segment (the β20 strand) displayed a broad and asymmetric ^{19}F NMR spectrum that can be deconvoluted into two peaks, the major S1 peak and a minor S1' peak. The S1 peak ($\Delta\nu_{S1}$) has an estimated line width of 85 Hz, which is similar to the single S1 peak observed at the equivalent site in βarr1 (81 Hz), indicating that it most probably corresponds to the β-strand conformation that docks into the N-domain groove. The S1' peak is more heterogeneous, showing a linewidth $\Delta\nu_{S1'}$ of 137 Hz. ^{19}F chemical exchange saturation transfer (CEST) experiment confirms an exchange

between the S1 and S1′ states, and the S1→S1′ transition rate is estimated to be 1.0 ± 0.4 s^{-1} (Fig. 1F–G). In comparison, the CEST profile of βarr1 F388C is more symmetric, showing no obvious minor state (Fig. 1F). Moreover, all three sites (N372C$^{\beta arr2}$, N379C$^{\beta arr2}$ and D384C$^{\beta arr2}$) in the proximal segment of βarr2 show systematic increased linewidths compared to their equivalents in βarr1 (N375C$^{\beta arr1}$, N382C$^{\beta arr1}$ and D384C$^{\beta arr1}$) (Fig. 1E). These observations suggest that the proximal-to-middle region of βarr2 C-tail exhibit elevated dynamics, sampling multiple conformations differing from the basal conformation.

In the V2Rpp-bound state, which mimics receptor tail engagement, significant differences were further observed between the βarr isoforms. In βarr1, V2Rpp binding induces the transition from the inactive S1 peak into the active S2 peak with significantly reduced linewidth for the F388C$^{\beta arr1}$ site ($\Delta\nu_{S1}$=81 Hz, $\Delta\nu_{S2}$=31 Hz), as well as for the D384C$^{\beta arr1}$ ($\Delta\nu_{S1}$=59 Hz, $\Delta\nu_{S2}$=34 Hz) and A392C$^{\beta arr1}$ ($\Delta\nu_{S1}$=60 Hz, $\Delta\nu_{S2}$=47 Hz) sites adjacently located up- and downstream of the β20 strand (Fig. 1D). These results coincide with V2Rpp-induced release of βarr1 C-tail into an overall free, highly flexible conformational state. In βarr2, however, the linewidths of D384C$^{\beta arr2}$ ($\Delta\nu_{S2}$=65 Hz) and F388C$^{\beta arr2}$ ($\Delta\nu_{S2}$=62 Hz) resonances in the V2Rpp-bound state are only modestly reduced relative to the basal state S1 peak, and they are twice the value of their equivalents in βarr1 (Fig. 1E). More intriguingly, the A392C$^{\beta arr2}$ resonance is so severely broadened upon V2Rpp binding that it nearly disappeared. The N372C$^{\beta arr2}$ and N379C$^{\beta arr2}$ S2 resonances also exhibited line broadening relative to their S1 peaks. Therefore, the C-tail of V2Rpp-activated βarr2 does not adopt a free, fully-released conformation like βarr1. Since we did not observe obvious differences in the oligomerization states between the two βarr isoforms based on dynamic light scattering data (Fig. S3), a plausible explanation for these NMR observations is that the βarr2 C-tail remains associated with the structural main body, or that it interchanges between free and main body-associated conformational states.

Robust β-to-α transition in the chameleon motif observed only in βarr2

A recently reported cryo-EM structure of bovine βarr2 revealed that the middle segment of its C-tail transits from the β-strand structure into a helical conformation that docks with the central crest when bound to the D6 receptor tail (*26*). To verify whether this is also the case for the human βarrs in solution and whether it accounts for the peculiar NMR observations, we

combined ^{19}F NMR with computer-aided structure predictions by AlphaFold3 (AF3) (*27*). Firstly, we used AF3 to predict structural models of V2Rpp–βarr1/2 complexes. For βarr2, over 80% of the models contain a helix in the C-tail that engages with the central crest, whereas the βarr1 C-tail adopts a free and disordered conformation in the majority of predictions (Fig. 2A, Fig. S4A). The predicted helix in βarr2 varies in length, with a relatively stable segment formed by residues D383–D401 (Fig. S4B–C). Moreover, while most predictions show a binding orientation same as Fig. 2A–B, models adopting a reverse binding pose also exist (Fig. S4B). While binding to the structural main body could increase the effective local correlation time (τ_{eff}) and thus the linewidth, we suspect the local binding heterogeneity is more likely the main contributor to the severe line broadening of the A392C$^{\beta arr2}$ resonance, since we are always able to observe ^{19}F signals for probes labeled in the rigid segments in the N and C domains (*21*). Secondly, we generated a series of βarr1/2 chimeras by substituting their C-tail proximal and distal segments, which differ not only in lengths but also in amino acid compositions between the two isoforms (Fig. 2C–D, Fig. S5A). We used AF3 to predict their structures in complex with V2Rpp, and we monitored their C-tail conformations at the A392C site by ^{19}F NMR. Intriguingly, the percentage of predicted structures displaying a free released C-tail conformation follows the order of βarr2 (16%) ≈ βarr1_P2D2 (12%) < βarr1_P2 (22%) < βarr1_D2 (59%) < βarr2_P1D1 (96%) ≈ βarr1 (88%), which is in agreement with the gradual change of the ^{19}F NMR spectra at the A392C site (Fig. 2C–D). For example, βarr2_P1D1 (βarr2 containing the proximal and distal C-tail segments from βarr1) shows an A392C ^{19}F spectrum essentially similar to βarr1, and *vice versa*. Moreover, βarr1_P2 or βarr1_D2, with only one segment substituted, exhibits partial A392C ^{19}F signal attenuation. These results strongly support the validity of the AF3 models, and also highlight the central role of the proximal and distal elements in regulating βarr C-tail dynamics.

To further verify the structural model, we performed single-molecule fluorescence resonance energy transfer (smFRET) experiments by labeling A392 in the C-tail and K157/K158 in the N-domain (Fig. 2E–F). Both βarr1 and βarr2 show a dominant high-FRET species in the basal state, consistent with the binding of the C-tail in the N-domain groove. However, while βarr1 shows a dominant low-FRET species in the V2Rpp-bound state, indicative of C-tail release, the FRET efficiency distribution between this fluorophore pair remains unchanged for βarr2, which

is consistent with the AF3 model (Fig. 2B, Fig. S6). To examine whether the central crest is indeed the docking site for the C-tail helix, we introduced ^{19}F labeling at the V71C (finger loop) and F245C (C loop) sites of βarr2, both of which are involved in helix binding in the AF3 models (Fig. 2B). Indeed, the ^{19}F resonances for both sites in βarr2, but not βarr1, show severe line broadening upon V2Rpp-binding, which is comparable to the βarr2 A392C site (Fig. 2G). Moreover, the model is further supported by the observation that binding to receptor TM core competitively triggers the release of βarr2 C-tail (*vide infra*).

Structural factors underlying the β-to-α transition in βarr2 C-tail

The above results demonstrate that both the proximal and distal segments of βarr C-tails contribute to modulating the dynamical behavior of the central chameleon sequence. To gain mechanistic insights, we analyzed the two segments separately.

The distal segment of βarr2 is shorter than βarr1 (7 *vs* 16 residues). In the AF3 predicted models of the V2Rpp–βarr2 complex, over half of the population display a long helix that extends all the way to the C-terminus. The βarr1 distal region contains a Gly/Pro-rich insertion ("ED**G**T**G**S**P**") that disfavors helix formation (Fig. S5C). We deleted this sequence from the βarr1_P2 construct, generating a βarr1_P2D1$^{\Delta GP}$ variant, which shows an A392C ^{19}F spectrum highly similar to both βarr1_P2D2 and βarr2. This result supports the suggestion that the Gly/Pro-rich motif inhibits β-to-α transition in βarr1.

The proximal segment appears to have a larger impact on C-tail dynamics, since the spectrum of βarr1_P2 variant is more similar to βarr2 than βarr1_D2 (Fig. 2C). The proximal segment in βarr2 is longer than βarr1 (38 *vs* 31 residues). Because it acts as a linker between the chameleon motif and the βarr main body, we speculate that the shorter length of βarr1 may be less favorable for the α-helix to reach out to the central crest. However, inserting seven Gly residues into the proximal region of βarr1 (βarr1_P1^{+7G} or βarr1_P1^{+7G}D1$^{\Delta GP}$) does not promote obvious helix formation (Fig. 2H), suggesting that linker length itself is not the major factor. We then compared the amino acid differences between the two isoforms and observed that the βarr2 proximal segment displays two unique features: (1) the N-terminal half of the segment contains more prolines and they show a more scattered distribution than βarr1 ("**P**L**P**R**P**QSSA**P**" *vs* "**PP**HREV**P**"); (2) the C-terminal half harbors a YAT motif immediately upstream of the

chameleon motif. Both features are conserved across different species (Fig. S7), and disruption of each of them (as in the βarr1_P2^{-Pro}D1$^{\Delta GP}$ or βarr1_P2^{-YAT}D1$^{\Delta GP}$ mutants) reintroduced βarr1-like C-tail dynamics compared to the βarr1_P2D1$^{\Delta GP}$ variant (Fig. 2H, Fig. S5). On one hand, the proline distribution pattern in βarr2 may be favorable for the linker to wrap around the N-domain, enabling the C-tail helix–central crest engagement. On the other hand, AF3-predicted models and molecular dynamics (MD) simulations of basal-state βarrs suggest that the YAT motif is favorable for forming a i→i+3 hydrogen bond (H-bond) between T382 of the YAT motif and D385 of the chameleon motif (Fig. 2I, Fig. S8). Combining this feature with the enhanced dynamics in the proximal-to-middle region in basal-state βarr2 (Fig. 1D–E), we speculate that the YAT motif may promote helix initiation and that the S1' resonance observed at the F388C$^{\beta arr2}$ site may represent a pre-formed local helical or an intermediate conformation. As expected, both βarr2$^{\Delta YAT}$ and βarr2^{T382N} mutants show a weakened S1-S1' exchange in the ^{19}F saturation transfer difference (STD) experiment at the F388C$^{\beta arr2}$ site, whereas the βarr2^{T382S} mutant preserving the H-bond still exhibits observable S1–S1' exchange (Fig. 2J).

Receptor core and membrane interactions release βarr2 C-tail

To further explore the βarr isoform differences in the tail- and core-engaged complexes with a full-length GPCR, we used the prototypical β_2AR with its C terminus replaced by that of V2R (β_2AR_{VC}). The receptor was phosphorylated ($p\beta_2AR_{VC}$) in cell by co-expression with GRK2, activated with isoproterenol (ISO), and reconstituted into 12-nm lipid nanodiscs.

To obtain the tail-engaged sample, $p\beta_2AR_{VC}$ was pre-incubated with excess miniGα_s protein to block its core binding site prior to the addition of βarrs. The A392C ^{19}F spectra of both βarrs acquired under this condition are highly similar to those in the V2Rpp-bound state. Addition of the membrane phosphatidylinositol 4,5-bisphosphate (PIP_2) has little effect on the βarr1 resonance, whereas it induces the appearance of a βarr2 S2 resonance with a linewidth of ~ 80 Hz. In the $p\beta_2AR_{VC}$ core-engaged state, prepared without the G protein, a βarr2 S2 resonance with a narrower linewidth (~60 Hz) was observed, whereas the narrowest βarr2 peak (~40 Hz) could be obtained when PIP_2 is added in the core-engaged sample (Fig. 3A-B). These results support the scenario of a competitive binding between the βarr2 C-tail (upon activation) and the receptor TM core, and suggest that receptor core and membrane PIP_2 interacts collectively

promote the release of βarr2 C-tail (Fig. 3C–D). The PIP_2-induced appearance of a broadened S2 peak in the miniGα_s-blocked, tail-engaged sample probably reflect partial C-tail release due to atypical membrane–central crest interactions, as recently suggested by multiple studies (*19, 20, 28-30*). Moreover, once the core-engaged β_2AR–βarr2 complex is formed, it remains relatively stable since addition of miniGα_s protein at this stage cannot revert the A392C ^{19}F spectrum (Fig. 3A).

Structures of the β_2AR–arrestin core-engaged complexes

The structures of the two β_2AR–βarr core-engaged complexes were further determined by cryo-EM. Similar to the NMR experiments, we assembled the complexes by reconstituting ISO-activated pβ_2AR_{VC} with full-length βarr1/βarr2 in nanodiscs, with the addition of antibody fragment Fab30 and nanobody Nb32. For β_2AR–βarr2 complex, we also added PIP_2 to gain higher data quality. Single particle analysis of the core-engaged conformation enabled us to obtain 3D maps of the β_2AR–βarr1 and β_2AR–βarr2 complexes at global resolutions of 3.06 Å and 3.03 Å, respectively (Fig. S9 and Table S1). Focused refinement on the receptor 7TM region in the β_2AR–βarr1 complex was performed to improve resolution. These maps enabled us to build the models of the receptor and βarrs with well-resolved features at the binding interface as well as in the receptor TM core (Fig. 4A-B and Fig. S10).

Binding to β_2AR in the core-engaged state involves two regions in βarrs. On one hand, the phosphorylated V_2R C terminus binds the arrestin N domain identical to previous structures (Fig. S11A-C). We are able to resolve six phosphates from the V_2R C terminus forming ionic interactions with the N domain, and we observe no obvious differences between βarr1 and βarr2 at this binding site (Fig. 4C). On the other hand, the finger loops of both βarrs insert into the receptor TM core, adopting an overall extended conformation. We observe that the βarr2 finger loop inserts slightly deeper and forms more contacts with residues in the receptor TM core (Fig. 4D, Fig. S12A-C). This is supported by monobromobimane (mBBr) fluorescence measurements labeled at the V70/V71 site of both βarrs (Fig. 4H). In the presence or absence of PIP_2, βarr2 exhibits a substantially larger fluorescence increase than βarr1 upon binding to pβ_2AR_{VC} (Fig. S12D), suggesting that the βarr2 finger loop resides in a more hydrophobic microenvironment in the receptor-complexed state, probably due to a more stable interaction at

this binding site.

Comparison between the β_2AR–βarr2 complex structure and the AF3-predicted model of activated βarr2 supports that the C-tail α-helix docking site overlaps with the binding interface with receptor TM3, TM5 and ICL2 (Fig. 4E). In particular, receptor ICL2 forms a short helix and engages in extensive contacts with the central crest, especially by inserting F139$^{34.51}$ (Ballesteros-Weinstein nomenclature) into a hydrophobic pocket formed by βarr2 I242, L244 and Y250 in the C loop and F62 in the β-strand preceding the finger loop (Fig. 4F). This is consistent with the NMR observation that receptor binding promotes βarr2 CT release. A recent cryo-EM structure of GPR1–βarr2 complex reveals the presence of a CHS molecule sandwiched between the receptor ICL2 and arrestin central crest (*19*). In our structure, no obvious densities were observed that would suggest the presence of a lipid molecule or an unreleased βarr2 CT. Instead, the density of a PIP_2 molecule could be identified at its canonical binding site (Fig. 4A).

In addition, utilization of large nanodiscs allows us to visualize βarr–membrane interactions via the C-edge loops (Fig. 4A–B, G). The C-edge loop 2 (residues 330–340) of βarr1, enriched in hydrophobic residues, inserts deeper into the lipid bilayer. βArr2 C-edge lacks the hydrophobic segment in loop 2, and mainly relies on hydrophobic residues L192 and M193 in loop 1 to anchor onto the membrane. The differences in C-edge loop–membrane contacts of the two βarr isoforms were also verified by mBBr fluorescence experiments (Fig. 4H). Consequently, βarr1 adopts a binding geometry with its C domain more tilted towards the membrane plane than βarr2 (Fig. 4I). Comparison with other GPCR–βarr structures (*11-17, 19*) demonstrates substantial variability of the tilt angle, which may be partially due to the use of detergent micelles for most of the complexes reported (Fig. S11D-E). Nevertheless, all structures suggest the strong tendency of βarr1 C-edge to bind to lipid environment. In addition, while βarr1 has been observed to pack to receptor TM core with distinct orientations, the β_2AR–βarr1/2 complexes reveal a packing orientation overall similar to a cluster of complexes, including the β_1AR–βarr1, GPR1–βarr1/2, μOR–βarr1, M_2R–βarr1 and CB1–βarr1 complexes (Fig. S11F-H).

Conformational changes in β_2AR transmembrane domain

Binding to βarrs induces the outward movement of TM6 — the hallmark of GPCR activation

— by 9.4 Å and 9.8 Å (by measuring the Cα of H269$^{6.31}$) relative to inactive β_2AR (PDB 2RH1). The displacement is slightly smaller than that observed in the Gs-engaged complex (12 Å, PDB 3SN6) (*31*). Moreover, while Gs binding induced a small outward movement of the cytoplasmic end of TM5, βarr coupling produced no obvious TM5 displacement. Moreover, the cytoplasmic ends of both TM5 and TM6 are observed to form longer helices in the Gs-engaged complex structure, presumably due to the more extensive contacts between receptor TM5/TM6 and Gs H5 helix (Fig. 4J). While both Gs and βarr-couplings induce inward movement of TM7, closer contacts were observed between the βarr finger loop and the TM7–H8 region in β_2AR in the βarr1/2-engaged complexes, accompanied by a more obvious counterclockwise rotation (viewed from the extracellular side) of TM7 near the NPxxY motif, forming a TM7 conformation distinct from the G-protein–coupled state (Fig. 4K). These observations coincide with the commonly suggested importance of TM7 in βarr-biased signaling (*32-35*).

Discussion

While growing evidences have highlighted functional distinctions between the two β-arrestins, the underlying molecular basis remains unclear. Previous comparative studies mainly focused on differences in the C-edge loops, which affect the βarr–membrane contact pattern and potentially modulate isoform-dependent receptor internalization and signaling (*20, 30, 36, 37*). However, little is known about how differences in the βarr C-tails contribute to functional divergence, partly because of their intrinsic flexibility and the fact that they are often unresolved in static structures. Herein we have combined multiple methods to explore the differences between human βarr1 and βarr2 in both receptor tail- and core-engaged states, unveiling distinct C-tail dynamics that were previously unrecognized.

Firstly, our results suggest that the proximal-to-middle segment of βarr2 C-tail shows elevated dynamics in the basal state, which is associated with conformational exchanges between major and minor conformations due to local helix-initiation. Since the middle segment (β20) autoinhibits βarr activation by docking into the phosphopeptide-binding cleft in the N domain, the higher sequence-encoded propensity to form local helix-like structures in βarr2 may lower the activation energetic barrier. This coincides with many previous functional studies that reported on higher-level activities of βarr2 in AP2 or clathrin binding, membrane recruitment,

and particularly in binding to and inducing the sequestration of class A receptors (e.g. β_2AR), which has an overall weaker and more transient interaction mode with βarrs (*6, 9, 38, 39*).

Secondly, we demonstrate that upon activation by phosphorylated V2R tail, the C-tail of βarr2 converts into a helical conformation and docks at the central crest. The fact that this state is broadened beyond NMR detection suggests that the binding is probably fuzzy. Besides V2Rpp, we also observed that activation by a phosphorylated peptide derived from the muscarinic M2 receptor 3rd intracellular loop (M2RICL3pp), which contains the consensus PxPP motif but has a shorter N-terminal end, also induced the disappearance of βarr2 A392C ^{19}F resonance, but not that of βarr1 (Fig. S13), supporting the idea that a robust C-tail helix formation is an intrinsic property of βarr2. This difference between βarr1 and βarr2 may have intriguing functional consequences. The βarr C-tail itself harbors protein-binding motifs essential for interactions with proteins in clathrin-coated pits (CCPs) (*40-43*). The proximal segment contains the clathrin-binding box, and chameleon middle segment is the binding site for the AP2 β2-appendage domain (Fig. 5). In the S* conformational state adopted by βarr2, both sites are presented on the protein surface facing towards the cellular membrane, which could be favorable for interactions with the endocytic CCP machinery (*42*). The dynamic nature of the helix–central crest interaction allows the helix to efficiently dissociate and engage with nearby AP2 molecules. Moreover, being an essential scaffold linking GPCRs to the MAPK signaling cascade, βarrs use various structural regions to bind different kinases, a process highly hierarchical and closely related to post-translational modifications of βarrs (*22, 44, 45*). For example, it has been suggested that MEK-mediated phosphorylation of T383 in βarr2 C-tail is crucial for Erk recruitment and activation, and it might require the C-tail to adopt a fully released conformation to place this site to the vicinity of the MEK active pocket (*22*). Therefore, the population equilibrium between the receptor tail-engaged and core-engaged conformations of βarr2 may play a role in fine-tuned regulation of the βarr-dependent MAPK signaling (Fig. 5).

Thirdly, by using nanodiscs with a large diameter, we are able to visualize for the first time the differences between the two isoforms in binding with the receptor TM core and the lipid membrane. Our results suggest that at a flat membrane surface, the two βarrs bind with different tilt angles, presumably due to the differences in their C-edge loops (Fig. 5). For βarr1, the

stronger anchoring of the C-edge loops into the membrane may compete against and destabilize the finger loop-TM core interaction due to a "seesaw-like" movement, thereby causing the finger loop to wobble out of the core binding site and adopt various atypical binding modes or form GPCR-G protein-β-arrestin megacomplex (*19, 20, 46, 47*). This scenario can be more prominent at a curved surface, such as the CCP, as demonstrated by recently reported structures of GPR1-βarr1 complexes (*19*). For βarr2, on the other hand, the weak C edge-membrane binding poses insignificant constraints on the finger loop-core interaction, resulting in a deeper and more stable insertion of the βarr2 finger loop, as suggested by both cryo-EM structures and fluorescence data.

Taken together, the differences between βarr1 and βarr2 in the C-tail dynamics and in the membrane-binding ability of the C-edge loops dramatically affect their conformational status in both receptor tail- and core-engaged complexes. Thus, the two βarr isoforms can have distinct spatial positioning, as well as accessibility, of their effector protein-binding sites or motifs, providing a framework to further elucidate the molecular mechanism underlying βarr isoform divergence in different cellular pathways, in response to different GPCR classes, and in different phases of signaling.

Materials and Methods

Expression and purification of βarrs

For expression and purification of human βarrs, we followed a previously reported protocol (*21*). Cysteine-less mutants of the long splice variant of human βarr1 (C59V/C125S/C140L/C150V/C242V/C251V/C269S) and human βarr2 (C17S/C60V/C126S/C141L/C151V/C243V/C252V/C270S) were used for introduction of single site cysteine mutation for ^{19}F labeling. The gene sequences were cloned into pET-28a(+) vector (Novagen) to introduce an N-terminal His-tag followed by a thrombin cleavage site, and transformed into *Escherichia coli* BL21(DE3) cells. The cells were cultured in TB medium containing 50 μg ml^{-1} kanamycin at 37 °C for 3 hours and then induced by 50 μM isopropyl-β-d-thiogalactopyranoside (IPTG) at 18 °C for 16 hours. The cells were harvested by centrifugation and resuspended in the lysis buffer (50 mM Tris-HCl, pH 8.0, 500 mM NaCl,

15% glycerol and APExBIO protease-inhibitor cocktail). Cells were lysed by sonication, followed by centrifugation. The supernatant was loaded onto a Ni Sepharose column (Cytiva), washed with the wash buffer (20 mM Tris-HCl, pH 8.0, 500 mM NaCl, 5% glycerol, 40 mM imidazole), and eluted with the elution buffer (20 mM Tris-HCl, pH 8.0, 500 mM NaCl, 5% glycerol, 250 mM imidazole). The eluate was collected and exchanged into the SEC buffer (20 mM Tris-HCl, pH 8.0, 150 mM NaCl) using PD-10 columns (Cytiva). The protein was concentrated using a 30-kDa molecular-weight-cutoff concentrator (Millipore) and then cleaved by thrombin to remove the His-tag. The protein was further purified by size-exclusion chromatography on a Superdex 200 Increase 10/300 GL column (Cytiva) pre-equilibrated with the SEC buffer. Peak fractions were pooled, concentrated to 5 mg ml^{-1}. The purified βarr samples were flash-frozen in liquid nitrogen and stored at −80 °C until use.

Expression and purification of miniG$_{\alpha s}$

The expression and purification of miniG$_{\alpha s}$ was performed following previously reported protocol (*48*). In brief, gene encoding the recombinant miniG$_{\alpha s}$ was cloned into pET-28a(+) vector (Novagen) to introduce an N-terminal His-tag followed by a HRV 3C protease cleavage site, and transformed into *E. coli* BL21(DE3) cells. The cells were cultured in TB medium containing 50 μg ml^{-1} kanamycin at 37 °C for 3 hours and then induced by 400 μM IPTG at 37 °C for 3 hours. Cells were harvested by centrifugation and resuspended in the lysis buffer (50 mM Tris-HCl, pH 8.0, 150 mM NaCl, 5 mM $MgCl_2$, 5 mM β-mercaptoethanol, 10 μM GDP). Cells were lysed by sonication, followed by centrifugation. The supernatant was loaded onto a Ni Sepharose column (Cytiva) and was washed with the wash buffer (50 mM HEPES, pH 8.0, 150 mM NaCl, 5 mM $MgCl_2$, 100 μM TCEP, 40 mM imidazole, 10% glycerol). The protein was eluted with the elution buffer (50 mM HEPES, pH 8.0, 150 mM NaCl, 5 mM $MgCl_2$, 100 μM TCEP, 300 mM imidazole, 10% glycerol). The eluate was collected and exchanged into the SEC buffer (20 mM Tris-HCl, pH 8.0, 150 mM NaCl) using PD-10 columns (Cytiva). The protein was concentrated using a 10-kDa molecular-weight-cutoff concentrator (Millipore), followed by His-tag removal using the HRV 3C protease. The protein was further purified by size-exclusion chromatography on a Superdex 75 Increase 10/300 GL column (Cytiva) pre-equilibrated with the SEC buffer. Peak fractions were pooled, concentrated to 10 mg ml^{-1}. The

purified mini$G_{\alpha s}$ was flash-frozen in liquid nitrogen and stored at −80 °C until use.

Expression and purification of Fab30

The expression and purification of Fab30 was performed following previously reported protocol (*4*). In brief, genes encoding the Fab30 heavy chain and light chains were cloned into the pETDuet-1 vector (Novagen) and transformed into *E. coli* BL21(DE3) cells. The cells were cultured in TB medium containing 100 μg ml^{-1} ampicillin at 37 °C for 3 hours and then induced by 500 μM IPTG at 18 °C for 16 hours. Cells were harvested by centrifugation and resuspended in the lysis buffer (50 mM HEPES, pH 8.0, 500 mM NaCl, 10% glycerol, 0.5% Triton X-100, 0.5 mM $MgCl_2$). Cells were lysed by sonication, and the lysate was heated at 65°C in a water bath for 30 min and immediately chilled on ice for 5 min. After centrifugation, the supernatant was loaded onto protein L column (GenScript) and was washed with the wash buffer (20 mM HEPES, pH 8.0, 500 mM NaCl). The protein was eluted with the elution buffer (100 mM glycine, pH 3.5), immediately neutralized to pH 8.0, and buffer-exchanged into the storage buffer (20 mM HEPES, pH 8.0, 100 mM NaCl). The protein was concentrated using a 30-kDa molecular-weight-cutoff concentrator (Millipore), supplemented with 10% glycerol, flash-frozen in liquid nitrogen and stored at −80 °C until use.

Expression and purification of Nb32

The expression and purification of Nb32 was performed following previously reported protocol (*49*). In brief, the gene encoding Nb32 was cloned into the pET-28a(+) vector (Novagen) to introduce an N-terminal His-tag and transformed into *E. coli* BL21(DE3) cells. The cells were cultured in LB medium containing 50 μg ml^{-1} kanamycin at 37 °C for 3 hours and then induced by 400 μM IPTG at 16 °C for 16 hours. Cells were harvested by centrifugation and resuspended in the lysis buffer (25 mM HEPES, pH 7.5, 150 mM NaCl). Cells were lysed by sonication, followed by centrifugation. The supernatant was loaded onto a Ni Sepharose column (Cytiva) and was washed with the wash buffer (25 mM HEPES, pH 7.5, 150 mM NaCl, 40 mM imidazole). The protein was eluted with the elution buffer (25 mM HEPES, pH 7.5, 150 mM NaCl, 250 mM imidazole). The eluate was collected and exchanged to the SEC buffer (25 mM HEPES, pH 7.5, 150 mM NaCl) using PD-10 columns. The protein was concentrated using a

3-kDa molecular-weight-cutoff concentrator (Millipore). The protein was further purified by size-exclusion chromatography on a Superdex 75 Increase 10/300 GL column (Cytiva) pre-equilibrated with a buffer containing the SEC buffer. Peak fractions were pooled, concentrated to 10 mg ml^{-1}. The purified Nb32 was flash-frozen in liquid nitrogen and stored at −80 °C until use.

Expression and purification of β_2AR_{VC}

The human β_2AR gene was cloned into the pFastBac vector (Invitrogen) with an N-terminal HA signal sequence followed by an M1-FLAG epitope. To improve expression and stability, the M96T, M98T, and N187E mutations were introduced, as commonly used in prior functional and structural studies (*50, 51*). The β_2AR C terminus (C341–L413) was replaced with the V2R fragment (A343–S371) to generate β_2AR_{VC}.

Phosphorylated β_2AR_{VC} was expressed with minor modifications from a previously described procedure (*4, 49*). Briefly, β_2AR_{VC} was expressed in *Spodoptera frugiperda* (*Sf9*; Expression Systems) insect cells using the baculovirus expression system. *Sf9* cells were co-infected with high-titer viral stocks of β_2AR_{VC} and GRK2-CAAX, a membrane-targeted GRK2 construct, at a multiplicity of infection ratio of 2:1. Isoproterenol was added to the culture medium to a final concentration of 10 μM 1 h before harvest. Cells were then collected and lysed as described previously (*50*). The receptor was solubilized from membranes in the solubilization buffer (20 mM HEPES, pH 7.4, 100 mM NaCl, 1% n-dodecyl-β-d-maltopyranoside (DDM), 0.03% cholesteryl hemisuccinate (CHS), 2 mM $MgCl_2$, 10 μM isoproterenol, APExBIO protease-inhibitor cocktail and phosphatase inhibitors). Membranes were first homogenized with a Dounce homogenizer, after which the soluble fraction was collected by centrifugation and incubated with M1 anti-FLAG immunoaffinity resin (Sigma-Aldrich). Resin-bound receptor was washed by the wash buffer (20 mM HEPES, pH 7.4, 350 mM NaCl, 0.1% DDM, 0.01% CHS, 10 μM isoproterenol, 2.5 μg ml^{-1} leupeptin, 160 μg ml^{-1} benzamidine). Detergent was then exchanged by washing the resin with a progressive DDM-to-LMNG gradient to reach 0.01% (w/v) lauryl maltose neopentyl glycol (LMNG) and 0.001% CHS. Receptor was eluted with the elution buffer (20 mM HEPES, pH 7.5, 100 mM NaCl, 0.01% LMNG/0.001% CHS, 10 μM isoproterenol, 0.2 mg ml^{-1} flag peptide and 5 mM EDTA), and further purified by size-exclusion

chromatography on a Superdex 200 Increase 10/300 GL column (Cytiva) in the SEC buffer (20 mM HEPES, pH 7.5, 100 mM NaCl, 0.01% LMNG/0.001% CHS, 10 μM isoproterenol). Purified β_2AR_{VC} was concentrated to 200 μM, supplemented with 20% glycerol, flash-frozen and stored at −80 °C.

Reconstitution of β_2AR_{VC} in nanodiscs

The MSP1D1E3 protein used for nanodisc assembly was expressed and purified as described previously (*13, 52*). In brief, the gene encoding the MSP1D1E3 was cloned into pET-28a(+) vector (Novagen) to introduce an N-terminal His-tag, and transformed into *E. coli* BL21(DE3) cells. The cells were cultured in TB medium containing 50 μg ml^{-1} kanamycin at 37 °C for 3 hours and then induced by 1 mM IPTG at 37 °C for 3 hours. Cells were harvested by centrifugation and resuspended in the lysis buffer (50 mM HEPES, pH 7.5, 300 mM NaCl, 100 mM KCl, protease inhibitor) and lysed by sonication. The lysate was supplemented with 1% Triton X-100. The supernatant was loaded onto a Ni Sepharose column (Cytiva), washed with the wash buffer (50 mM HEPES, pH 7.5, 300 mM NaCl, 100 mM KCl, 50 mM sodium cholate, 20 mM imidazole), and eluted with the elution buffer (20 mM Tris-HCl, pH 8.0, 300 mM NaCl, 100 mM KCl, 250 mM imidazole). The eluate was exchanged into the Q buffer (20 mM Tris-HCl, pH 8.0, 10 mM NaCl) and further purified using the Mono Q 10/100 GL column (Cytiva). Peak fractions were pooled, concentrated to 30 mg mL^{-1}, flash-frozen in liquid nitrogen, and stored at −80 °C until use.

β_2AR_{VC} was pre-incubated with a 10-fold molar excess of isoproterenol on ice for 30 min prior to reconstitution. The β_2AR_{VC} was then mixed with MSP1D1E3 and the POPC/POPG lipids at a molar ratio of 1:30:2000 on ice for 2 hours. The reconstitution was performed in buffer containing 20 mM HEPES (pH 7.5), 100 mM NaCl, and 0.5 mM EDTA. Detergent was removed using Bio-Beads (BioRad). The supernatant was incubated with M1 anti-FLAG immunoaffinity resin (Sigma-Aldrich), washed with a buffer containing 20 mM HEPES (pH 7.5), 100 mM NaCl, 10 μM isoproterenol, 2.5 μg ml^{-1} leupeptin, 160 μg ml^{-1} benzamidine, to isolate empty nanodiscs. β_2AR_{VC}-ND was eluted with the eluate buffer (20 mM HEPES, pH 7.5, 100 mM NaCl, 10 μM isoproterenol, 0.2 mg ml^{-1} flag peptide, and 5 mM EDTA) and further purified using the Superdex 200 Increase 10/300 GL column (Cytiva) in the SEC buffer

(20 mM HEPES, pH 7.5, 100 mM NaCl, 10 μM isoproterenol). β_2AR_{VC} reconstituted into nanodiscs (β_2AR_{VC}-ND) was concentrated to 100 μM, supplemented with 20% glycerol, flash-frozen in liquid nitrogen, and stored at −80 °C. Unless otherwise indicated, all β_2AR_{VC} samples in subsequent experiments refer to β_2AR_{VC}-ND.

Synthetic peptides

The V2Rpp peptide (ARGRpTPPpSLGPQDEpSCpTpTApSpSpSLAKDTSS), derived from the phosphorylated C terminus of the human V2 vasopressin receptor, was synthesized by the Tufts University Core Facility. The M2RICL3pp peptide (TQDENpTVpSpTpSLGHSKDENSKQT), derived from the phosphorylated intracellular loop 3 (ICL3) of the human M2 muscarinic receptor, was synthesized by Scilight-Peptide.

^{19}F labeling of βarrs

Single-cysteine βarrs mutants were adjusted to 50 μM for labeling with the sulfoxide-based ^{19}F probe wPSP-6F (*53*). The wPSP-6F stock was added at a 5-fold molar excess in the presence of 100 μM TCEP, and the reaction was incubated at 4°C for 1 h. Labeling was quenched by addition of dithiothreitol. Samples were then exchanged into the SEC buffer (20 mM Tris-HCl, pH 8.0, 150 mM NaCl) to remove unreacted small molecules and further purified by a second round of size-exclusion chromatography. Peak fractions were pooled, concentrated to 100 μM, flash-frozen in liquid nitrogen, and stored at −80 °C until use. Sample purity was assessed by SDS-PAGE.

Preparation of ^{19}F-NMR samples of βarrs in different states

All βarrs ^{19}F NMR samples were prepared in NMR buffer to a final volume of 135 μL, containing 20 mM Tris-HCl (pH 8.0), 150 mM NaCl, 2.5 μg mL^{-1} leupeptin, 160 μg mL^{-1} benzamidine, protease-inhibitor cocktail (Roche), 10% D_2O for the field lock, and 1 μM sodium trifluoroacetate (STFA) as an internal chemical shift reference. Samples were sterile-filtered, transferred into sterile 3-mm NMR microtubes, and maintained under a nitrogen atmosphere to minimize microbial contamination.

For V2Rpp-bound samples, V2Rpp peptide was added at a 2-fold molar excess relative to βarrs.

For M2RICL3pp-bound samples, M2RICL3pp peptide was added at a 4-fold molar excess relative to βarrs. For β_2AR_{VC}-bound samples, complexes were prepared at a $\beta_2AR_{VC:}$ βarrs molar ratio of 1.5:1. In addition, 0.5 mM isoproterenol was included to maintain the receptor in an active state, and 1 mM ascorbic acid was added to prevent ligand oxidation. In the presence of PIP_2, diC8-PtdIns(4,5)P_2 was added at a 3:1 molar ratio relative to βarrs. For preparation of tail-engaged samples, β_2AR_{VC} was first incubated with a 3-fold molar excess of mini$G_{\alpha s}$ at room temperature for 30 min, followed by addition of 0.1 U apyrase and overnight incubation at 4 °C to stabilize mini$G_{\alpha s}$ binding to the receptor core. βArrs was then added to the samples at the desired $\beta_2AR_{VC:}$ βarrs ratio (1.5:1). Final βarrs concentrations for ^{19}F NMR experiments were 10–30 μM. Unless otherwise noted, all complexes were incubated at 25°C for 1 h, and freshly prepared samples were immediately subjected to ^{19}F NMR measurements.

1D ^{19}F NMR experiments and data analysis

All ^{19}F NMR spectra were recorded at 298 K using a Bruker AVANCE III HD 800 MHz spectrometer equipped a ^{1}H-^{19}F/^{13}C/^{15}N TCI triple resonance cryogenic probe. All data were acquired and processed using the Bruker Topspin 4.2.0 software. For all 1D ^{19}F NMR experiments, the traditional one-pulse sequence was used. The carrier frequency was set to −67.4 ppm and the spectra were recorded with 4k points and a spectral width of 15,000 Hz. SDS-PAGE were run for all samples before and after NMR experiments to ensure that no protein degradation occurs during the experiments. All NMR data were analyzed using the MestraNova 14.0.0 software. The ^{19}F chemical shifts were referenced to STFA at −75.45 ppm. The spectra were subsequently fitted iteratively using an LB value of 20 Hz.

For the ^{19}F NMR experiments on the A392C site of βarrs mutants, basal-state and V2Rpp-bound state samples were collected parallelly using the same batch of sample with identical protein concentration and spectrometer setup. The basal-state S1 peak was used as a reference to normalize and quantify the V2Rpp-bound S2 peak intensity among different βarr mutants.

^{19}F CEST and ^{19}F STD experiments

The ^{19}F CEST and ^{19}F STD experiments for the F388C site were acquired at 298 K using a Bruker AVANCE III HD 800 MHz spectrometer equipped a ^{1}H-^{19}F/^{13}C/^{15}N TCI triple resonance

cryogenic probe. Sample preparation was the same as for the 1D ^{19}F NMR experiments, and the protein concentrations were 50–100 μM.

For ^{19}F CEST experiments, a series of 1D saturation transfer experiments were recorded using a 0.2 s recovery delay followed by a 1.8 s saturation period using irradiation field strengths $\mathbf{B_1}$ of 5 Hz. The positions and spacings of the carrier frequencies for saturation were determined based on the signals observed in the 1D ^{19}F spectra, normally covering the chemical shift ranges of F388C S1 and S1′ signals. The spectra were processed and analyzed using the Bruker Topspin 4.2.0 and MestraNova 14.0.0 software.

^{19}F STD experiments and kinetic analysis were performed essentially as described previously (*54*). A series of time courses (12 points) were applied both at an on-resonance frequency (S1′) and at an off-resonance frequency ($\Delta\delta_{S1-S1'}$ relative to the S1, ctrl), to assess chemical exchange during steady-state saturation and off-resonance saturation effects. The $k_{S1-S1'}$ value was obtained by fitting to a two-state model.

smFRET experiments and data analysis

For smFRET experiments, βarrs constructs were generated on cysteine-less βarr background and engineered to include an N-terminal His-tag followed by an SSG linker, an AviTag, and a GGSGGS linker. Fluorophore labeling sites were introduced by point mutation (βarr1: K157C and A392C; βarr2: K158C and A392C). Protein expression and purification were performed as described above. After SEC, βarrs were biotinylated with recombinant BirA enzyme and further purified on a Superdex 200 Increase 10/300 GL column (Cytiva) in a buffer containing 20 mM Tris-HCl (pH 8.0) and 150 mM NaCl. Fluorophore labeling was performed by diluting βarrs to a concentration of 20 μM and reacting with 200 μM Cy3-maleimide and 200 μM Cy5-maleimide in the presence of 100 μM TCEP at 4 °C for 1 h. Excess dyes were removed by two sequential passes through PD-10 desalting columns (Cytiva).

All smFRET measurements were performed at room temperature on a home-built objective-type TIRF microscope based on a Nikon Eclipse Ti-E, equipped with an EMCCD camera (Andor iXon Ultra 897) and 532-nm and 640-nm solid-state lasers. Glass slides were passivated with a mixture of mPEG-SVA and biotin-PEG-SC and sequentially incubated with streptavidin. Cy3/Cy5-labeled and biotinylated βarrs were immobilized on the slide surface. Imaging buffer

contained 20 mM HEPES (pH 7.5), 100 mM NaCl, 50 nM protocatechuate-3,4-dioxygenase, 2.5 mM protocatechuic acid, 1.5 mM 6-hydroxy-2,5,7,8-tetramethyl-chromane-2-carboxylic acid, 1 mM 4-nitrobenzyl alcohol, and 1 mM cyclooctatetraene. To prepare V2Rpp-bound samples, V2Rpp (300 μM) was added into βarr samples and incubate at room temperature for 30 min; the imaging buffer for this condition also contained 300 μM V2Rpp.

Movies were recorded using Cell Vision software (Beijing Coolight Technology) with a 100-ms integration time and analyzed using a custom Python script. Donor and acceptor channels were aligned using the average of the first 10 frames of each movie. Fluorescence intensities were extracted from a 5 × 5 pixel region centered on each spot, with background estimated from a surrounding ring (16 pixels), and background-subtracted. Apparent FRET efficiency was calculated as $E = D_A / (D_A + D_D)$, where D_A and D_D are the acceptor- and donor-emission signals under donor excitation. Traces were truncated at the first detected photobleaching event and filtered in the script by requiring bleaching after the initial frames (break index > 10), stable total intensity over time, low donor–acceptor correlation, and sufficient signal-to-noise ratio.

Bimane fluorescence experiments

For mBBr fluorescence experiments, βarrs constructs were expressed and purified following the same protocols used for ^{19}F-labeled samples. βArr1 V70C, βarr1 L191C, βarr1 L334C, βarr2 V71C, βarr2 L192C, and βarr2 G334C mutants were generated via site-directed mutagenesis. The purified βarrs were fluorescently labeled by incubating with a 10-fold molar excess of mBBr at 4 °C overnight. The labeling reaction and all subsequent procedures were performed in the dark. The labeled samples were then loaded onto a Superdex 200 Increase 10/300 GL column (Cytiva) using a buffer containing 20 mM Tris-HCl (pH 8.0) and 150 mM NaCl to remove free probes. Peak fractions were pooled and concentrated to 5 mg mL^{-1}.

The mBBr-labeled βarrs were diluted to 1 μM and incubated with 3 μM β_2AR_{VC} or 3 μM empty nanodisc at room temperature for 30 minutes, with 100 μM isoproterenol added. For PIP_2-containing conditions, 4.5 μM diC8-PtdIns(4,5)P_2 was included. The buffer consisted of 20 mM HEPES (pH 7.5) and 100 mM NaCl. Reactions were transferred to a 384-well black plate (Corning) for fluorescence measurements using a plate reader (BioTek). The excitation wavelength was set to 375 nm (16-nm bandpass), and fluorescence was monitored from 420 to

600 nm (10-nm bandpass) in 2-nm increments. The measurements were repeated six times. Statistics were calculated by comparing the area under the curves (430–540 nm) using GraphPad Prism 10.

DLS Analysis

DLS measurements were performed to assess protein size using a DynaPro NanoStar instrument. βArrs was measured at a concentration of 0.5 mg mL^{-1} in 20 mM Tris-HCl (pH 8.0) and 150 mM NaCl, in the absence or presence of V2Rpp added at a 2-fold molar excess relative to βarrs. Samples were loaded into disposable cuvettes and measured at 25 °C. Data were analyzed by considering particles with diameters < 200 nm, and average diameter distributions were determined. Each sample was measured with seven technical replicates.

Cryo-EM sample preparation and data acquisition

Nanodisc-reconstituted β_2AR_{VC} was pre-incubated for 30 min with 10-fold molar excess of isoproterenol. Then, 1.5-fold molar excess of full-length βarr1 or βarr2 was added and incubated at room temperature for 30 min, followed by addition of 2-fold molar excess of Fab30 and 5-fold molar excess of Nb32 for another 30 min. The supernatant was incubated with M1 anti-FLAG immunoaffinity resin (Sigma-Aldrich) and washed with a buffer containing 20 mM HEPES (pH 7.5), 100 mM NaCl, 10 μM isoproterenol, and protease inhibitors to remove unbound proteins. The complex was eluted with the eluate buffer (20 mM HEPES, pH 7.5, 100 mM NaCl, 10 μM isoproterenol, 0.2 mg ml^{-1} flag peptide, and 5 mM EDTA) and further purified by size-exclusion chromatography on a Superdex 200 Increase 10/300 GL column (Cytiva) in the SEC buffer (20 mM HEPES, pH 7.5, 100 mM NaCl, 10 μM isoproterenol). Complex purity and homogeneity were assessed by SDS-PAGE. The complex was concentrated to 6.5 mg mL^{-1} for cryo-EM analysis.

For the cryo-EM experiments, 3 μL of the purified protein complex were applied onto holy-carbon gold grids (Quantifoil, R1.2/1.3). The grids were blotted in Vitrobot Mark IV (FEI) with blot time of 1.5 s and blot force of −2, and then plunged into frozen liquid ethane, with the chamber condition maintained to 4 °C temperature and 100% humidity. After vitrification, the grids were transferred, stored in liquid nitrogen, and used for further analysis.

The cryo-grids were screened on a 200 kV Talos Arctica microscope equipped with a K2 summit direct electron detector (Thermo Fisher Scientific). All images were recorded with a BioQuantum K3 direct detector (Gatan) in the super-resolution. The nominal magnification was set to 81,000×, resulting in a calibrated physical pixel size of 1.07 Å. Movies were recorded with a total exposure time of 3.84 s, fractionated into 32 frames, with the total dose set to 60 e/Å^2 and a dose rate of 17.9 e/pixel/s. The defocus range was set from −1.0 to −1.5 μm. Movies were used in this study were collected automatically using the EPU software.

Cryo-EM data processing and model building

Cryo-EM image processing was performed using cryoSPARC v4.4.1 (*55*) and RELION v4.0.1 (*56*). Movies were subjected to beam-induced motion correction using Patch MotionCorr in cryoSPARC with a binning factor of 2, yielding a calibrated pixel size of 1.07 Å. Contrast transfer function (CTF) parameters were estimated using Patch CTF.

For the β_2AR_{VC}-βarr1 and β_2AR_{VC}-βarr2 datasets, 5,796 and 9,600 micrographs were collected, respectively, and 2,065,492 and 3,896,616 particles were blob-picked and subjected to several rounds of ab-initio reconstruction, heterogeneous refinement and 2D classification. The best-resolved classes were then subjected to non-uniform refinement to generate templates for particle picking. Template-based picking yielded a total of 6,125,640 particles for β_2AR_{VC}-βarr1 and 42,132,418 particles for β_2AR_{VC}-βarr2. Following a series of 2D and 3D classifications, ab-initio reconstruction, and heterogeneous refinement to remove junk particles, final subsets of 123,512 and 242,296 particles were selected for the final refinement of β_2AR_{VC}-βarr1 and β_2AR_{VC}-βarr2, yielding density maps at resolutions of 3.06 Å and 3.03 Å, respectively. To further improve the map quality of β_2AR_{VC}-βarr1 surrounding the density of trans-membrane domain for subsequent model building, local CTF refinement was performed in RELION, and the final maps were post-processed using DeepEMhancer (*57*).

Initial models were generated using AlphaFold 3 (server implementation) (*27*). These predicted templates were docked into the density maps using Chimera and subsequently subjected to iterative rounds of manual adjustment in Coot (*58*). For β_2AR_{VC}-βarr1, the enhanced density map was used to accurately refine the modeling of the transmembrane domain. The final models were subjected to real-space refinement against the maps using Phenix (*59*) and the structural

geometries of the final models were evaluated using MolProbity (*60*).

Conformational ensemble generation by AlphaFold3

Conformational ensemble models of βarrs and the chimeras in complex with V2Rpp were generated using AF3 (*27*). The resulting ensembles were used to characterize C-tail conformational distributions under activation conditions. To improve sampling of activated C-tail conformations, modeling was performed on the βarr1 R169E / βarr2 R170E background. For each chimera, multiple models were generated using different random seeds, yielding 115 conformations in which the C-tail was released from the N-domain. Models were ranked by AF3 ranking score, and the top 80% were retained for analysis. Within the V2Rpp–βarrs ensemble, we quantified the population of models in which the C-tail adopted a disordered, coil-like conformation (free state).

Basal-state βarrs ensembles were generated independently using different random seeds (100 models total), followed by ranking score-based selection of the top 80%.

Molecular dynamics simulations

Molecular dynamics simulations were performed using the AF3-generated structures as the starting models (*27*). Initial simulation conditions were set up using the CHARMM-GUI (www.charmm-gui.org). The system was solvated with TIP3P water and 0.15 M NaCl and simulated with GROMACS 2020.3 using the CHARMM36m force field (*61*) under periodic boundary conditions. Following energy minimization, the system was equilibrated using a staged heating and stepwise restraint-release protocol, following previously described simulation workflows (*62*), consisting of an NVT run at 100 K for 12.5 ps, an NPT heating phase from 100 to 310 K for 125 ps, and subsequent NPT equilibration at 310 K and 1 bar with gradually released backbone position restraints, followed by a final NPT equilibration without restraints. Production simulations were performed in the NPT ensemble at 310 K and 1 bar using the velocity-rescale thermostat and the Parrinello–Rahman barostat. Long-range electrostatics were treated with particle mesh Ewald (PME), and van der Waals interactions used a force-switch scheme. Bond lengths involving hydrogen atoms were constrained using LINCS (*63*), and hydrogen mass repartitioning was applied to enable a 4 fs integration timestep

(*64*). Non-bonded interactions were handled using the Verlet cutoff scheme with PME for electrostatics, with a real-space cutoff of 1.2 nm. A force-switching scheme was applied to the Lennard–Jones interactions, with a cutoff between 1.0 and 1.2 nm.

References

1. W. I. Weis, B. K. Kobilka, The molecular basis of G protein-coupled receptor activation. *Annu. Rev. Biochem.* **87**, 897–919 (2018).
2. S. M. DeWire, S. Ahn, R. J. Lefkowitz, S. K. Shenoy, Beta-arrestins and cell signaling. *Annu. Rev. Physiol.* **69**, 483–510 (2007).
3. D. Hilger, M. Masureel, B. K. Kobilka, Structure and dynamics of GPCR signaling complexes. *Nat. Struct. Mol. Biol.* **25**, 4–12 (2018).
4. A. K. Shukla *et al.*, Visualization of arrestin recruitment by a G-protein-coupled receptor. *Nature* **512**, 218–222 (2014).
5. T. J. Cahill *et al.*, Distinct conformations of GPCR-β-arrestin complexes mediate desensitization, signaling, and endocytosis. *Proc. Natl. Acad. Sci. U.S.A.* **114**, 2562–2567 (2017).
6. T. A. Kohout, F. S. Lin, S. J. Perry, D. A. Conner, R. J. Lefkowitz, beta-Arrestin 1 and 2 differentially regulate heptahelical receptor signaling and trafficking. *Proc. Natl. Acad. Sci. U.S.A.* **98**, 1601–1606 (2001).
7. S. Ahn, C. D. Nelson, T. R. Garrison, W. E. Miller, R. J. Lefkowitz, Desensitization, internalization, and signaling functions of beta-arrestins demonstrated by RNA interference. *Proc. Natl. Acad. Sci. U.S.A.* **100**, 1740–1744 (2003).
8. S. Ahn, H. Wei, T. R. Garrison, R. J. Lefkowitz, Reciprocal regulation of angiotensin receptor-activated extracellular signal-regulated kinases by beta-arrestins 1 and 2. *J. Biol. Chem.* **279**, 7807–7811 (2004).
9. A. Srivastava, B. Gupta, C. Gupta, A. K. Shukla, Emerging functional divergence of beta-arrestin isoforms in GPCR function. *Trends Endocrinol. Metab.* **26**, 628–642 (2015).
10. W. Yin *et al.*, A complex structure of arrestin-2 bound to a G protein-coupled receptor. *Cell Res.* **29**, 971–983 (2019).
11. W. Huang *et al.*, Structure of the neurotensin receptor 1 in complex with β-arrestin 1. *Nature* **579**, 303–308 (2020).
12. Y. Lee *et al.*, Molecular basis of β-arrestin coupling to formoterol-bound β1-adrenoceptor. *Nature* **583**, 862–866 (2020).
13. D. P. Staus *et al.*, Structure of the M2 muscarinic receptor-β-arrestin complex in a lipid nanodisc. *Nature* **579**, 297–302 (2020).
14. J. Bous *et al.*, Structure of the vasopressin hormone-V2 receptor-β-arrestin1 ternary complex. *Sci. Adv.* **8**, eabo7761 (2022).
15. C. Cao *et al.*, Signaling snapshots of a serotonin receptor activated by the prototypical psychedelic LSD. *Neuron* **110**, 3154–3167.e7 (2022).
16. Y.-Y. Liao *et al.*, Snapshot of the cannabinoid receptor 1-arrestin complex unravels the biased signaling mechanism. *Cell* **186**, 5784–5797.e17 (2023).
17. H. Zhang *et al.*, The molecular basis of μ-opioid receptor signaling plasticity. *Cell Res.* **35**,

1021–1036 (2025).
18. K. Chen *et al.*, Tail engagement of arrestin at the glucagon receptor. *Nature* **620**, 904–910 (2023).
19. H. Cai *et al.*, Noncanonical agonist-dependent and -independent arrestin recruitment of GPR1. *Science* **390**, eadt8794 (2025).
20. Q. Chen *et al.*, Effect of phosphorylation barcodes on arrestin binding to a chemokine receptor. *Nature* **643**, 280–287 (2025).
21. R. Zhai *et al.*, Distinct activation mechanisms of β-arrestin-1 revealed by ^{19}F NMR spectroscopy. *Nat. Commun.* **14**, 7865 (2023).
22. E. Cassier *et al.*, Phosphorylation of β-arrestin2 at Thr383 by MEK underlies β-arrestin-dependent activation of Erk1/2 by GPCRs. *eLife* **6**, e23777 (2017).
23. W. B. Asher *et al.*, GPCR-mediated β-arrestin activation deconvoluted with single-molecule precision. *Cell* **185**, 1661–1675.e16 (2022).
24. V. V. Gurevich, E. V. Gurevich, GPCR-dependent and -independent arrestin signaling. *Trends Pharmacol. Sci.* **45**, 639–650 (2024).
25. I. Petrovic *et al.*, A high-resolution analysis of arrestin2 interactions responsible for CCR5 endocytosis. *eLife* **14**, RP106839 (2026).
26. J. Maharana *et al.*, Molecular insights into atypical modes of β-arrestin interaction with seven transmembrane receptors. *Science* **383**, 101–108 (2024).
27. J. Abramson *et al.*, Accurate structure prediction of biomolecular interactions with AlphaFold 3. *Nature* **630**, 493–500 (2024).
28. J. Grimes *et al.*, Plasma membrane preassociation drives β-arrestin coupling to receptors and activation. *Cell* **186**, 2238–2255.e20 (2023).
29. A. A. S. Gomes *et al.*, Lipids modulate the dynamics of GPCR:β-arrestin interaction. *Nat. Commun.* **16**, 4982 (2025).
30. T. D. Killeen *et al.*, Distinct membrane binding properties of the two non-visual arrestins. *Commun. Biol.* **9**, 150 (2026).
31. S. G. F. Rasmussen *et al.*, Crystal structure of the β2 adrenergic receptor-Gs protein complex. *Nature* **477**, 549–555 (2011).
32. J. J. Liu, R. Horst, V. Katritch, R. C. Stevens, K. Wüthrich, Biased signaling pathways in beta2-adrenergic receptor characterized by ^{19}F-NMR. *Science* **335**, 1106–1110 (2012).
33. C.-M. Suomivuori *et al.*, Molecular mechanism of biased signaling in a prototypical G protein-coupled receptor. *Science* **367**, 881–887 (2020).
34. Q. Qu *et al.*, Insights into distinct signaling profiles of the μOR activated by diverse agonists. *Nat. Chem. Biol.* **19**, 423–430 (2022).
35. V. A. Rangari *et al.*, A cryptic pocket in CB1 drives peripheral and functional selectivity. *Nature* **640**, 265–273 (2025).
36. Q. Chen *et al.*, An Eight amino acid segment controls oligomerization and preferred conformation of the two non-visual arrestins. *J. Mol. Biol.* **433**, 166790 (2021).
37. R. S. Haider *et al.*, β-arrestin1 and 2 exhibit distinct phosphorylation-dependent conformations when coupling to the same GPCR in living cells. *Nat. Commun.* **13**, 5638 (2022).
38. R. H. Oakley, S. A. Laporte, J. A. Holt, M. G. Caron, L. S. Barak, Differential affinities of visual arrestin, beta arrestin1, and beta arrestin2 for G protein-coupled receptors delineate two major classes of receptors. *J. Biol. Chem.* **275**, 17201–17210 (2000).
39. M. O'Hayre *et al.*, Genetic evidence that β-arrestins are dispensable for the initiation of β2-

adrenergic receptor signaling to ERK. *Sci. Signal.* **10**, eaal3395 (2017).

40. S. A. Laporte, W. E. Miller, K.-M. Kim, M. G. Caron, beta-Arrestin/AP-2 interaction in G protein-coupled receptor internalization: identification of a beta-arrestin binding site in beta 2-adaptin. *J. Biol. Chem.* **277**, 9247–9254 (2002).
41. Y.-M. Kim, J. L. Benovic, Differential roles of arrestin-2 interaction with clathrin and adaptor protein 2 in G protein-coupled receptor trafficking. *J. Biol. Chem.* **277**, 30760–30768 (2002).
42. E. M. Schmid *et al.*, Role of the AP2 beta-appendage hub in recruiting partners for clathrin-coated vesicle assembly. *PLoS Biol.* **4**, e262 (2006).
43. D. S. Kang *et al.*, Structure of an arrestin2-clathrin complex reveals a novel clathrin binding domain that modulates receptor trafficking. *J. Biol. Chem.* **284**, 29860–29872 (2009).
44. L. M. Luttrell *et al.*, Activation and targeting of extracellular signal-regulated kinases by beta-arrestin scaffolds. *Proc. Natl. Acad. Sci. U.S.A.* **98**, 2449–2454 (2001).
45. A. W. Kahsai *et al.*, Signal transduction at GPCRs: Allosteric activation of the ERK MAPK by β-arrestin. *Proc. Natl. Acad. Sci. U.S.A.* **120**, e2303794120 (2023).
46. A. R. B. Thomsen *et al.*, GPCR-G protein-β-arrestin super-complex mediates sustained G protein signaling. *Cell* **166**, 907–919 (2016).
47. G. He *et al.*, A GPCR-G protein-β-arrestin megacomplex enabled by a versatile allosteric modulator. *Cell* **189**, 1434–1450.e22 (2026).
48. B. Carpenter, C. G. Tate, Expression and purification of mini G proteins from *Escherichia coli*. *Bio Protoc.* **7**, e2235 (2017).
49. A. H. Nguyen *et al.*, Structure of an endosomal signaling GPCR-G protein-β-arrestin megacomplex. *Nat. Struct. Mol. Biol.* **26**, 1123–1131 (2019).
50. J. Heng *et al.*, Function and dynamics of the intrinsically disordered carboxyl terminus of β2 adrenergic receptor. *Nat. Commun.* **14**, 2005 (2023).
51. M. Casiraghi *et al.*, Structure and dynamics determine G protein coupling specificity at a class A GPCR. *Sci. Adv.* **11**, eadq3971 (2025).
52. I. G. Denisov, Y. V. Grinkova, A. A. Lazarides, S. G. Sligar, Directed self-assembly of monodisperse phospholipid bilayer nanodiscs with controlled size. *J. Am. Chem. Soc.* **126**, 3477–3487 (2004).
53. Z. Chai *et al.*, Visualizing proteins in human cells at near-physiological concentrations with sensitive ^{19}F NMR chemical tags. *Angew. Chem. Int. Ed.* **62**, e202300318 (2023).
54. L. Ye, N. Van Eps, M. Zimmer, O. P. Ernst, R. S. Prosser, Activation of the A2A adenosine G-protein-coupled receptor by conformational selection. *Nature* **533**, 265–268 (2016).
55. A. Punjani, J. L. Rubinstein, D. J. Fleet, M. A. Brubaker, cryoSPARC: algorithms for rapid unsupervised cryo-EM structure determination. *Nat. Methods* **14**, 290–296 (2017).
56. S. H. Scheres, RELION: implementation of a Bayesian approach to cryo-EM structure determination. *J. Struct. Biol.* **180**, 519–530 (2012).
57. R. Sanchez-Garcia *et al.*, DeepEMhancer: a deep learning solution for cryo-EM volume post-processing. *Commun. Biol.* **4**, 874 (2021).
58. P. Emsley, K. Cowtan, Coot: model-building tools for molecular graphics. *Acta Crystallogr. D Biol. Crystallogr.* **60**, 2126–2132 (2004).
59. P. D. Adams *et al.*, PHENIX: a comprehensive Python-based system for macromolecular structure solution. *Acta Crystallogr. D Biol. Crystallogr.* **66**, 213–221 (2010).
60. C. J. Williams *et al.*, MolProbity: More and better reference data for improved all-atom structure

validation. *Protein Sci.* **27**, 293–315 (2018).
61. J. Huang *et al.*, CHARMM36m: an improved force field for folded and intrinsically disordered proteins. *Nat. Methods* **14**, 71–73 (2017).
62. N. R. Latorraca *et al.*, How GPCR phosphorylation patterns orchestrate arrestin-mediated signaling. *Cell* **183**, 1813–1825.e18 (2020).
63. B. Hess, P-LINCS: A parallel Linear constraint solver for molecular simulation. *J. Chem. Theory Comput.* **4**, 116–122 (2008).
64. C. W. Hopkins, S. Le Grand, R. C. Walker, A. E. Roitberg, Long-time-step molecular dynamics through hydrogen mass repartitioning. *J. Chem. Theory Comput.* **11**, 1864–1874 (2015).

Acknowledgements: All NMR experiments were performed at the Beijing NMR Center and the NMR facility of National Center for Protein Sciences at Peking University. Our work was supported by the cryo-EM Platform of Peking University and we would be grateful to Dr. Guopeng Wang for his help in EM sample preparation and EM image acquisition/analysis. We thank Dr. Zhaofei Chai from the Innovation Academy for Precision Measurement Science and Technology, Chinese Academy of Sciences for providing the ^{19}F probe. We thank Dr. Jintao Liu from Peking University for help with smFRET data analysis. We thank Dr. Zhou Gong from the Innovation Academy for Precision Measurement Science and Technology, Chinese Academy of Sciences for help in MD simulation setup.

Funding: This work was supported by the National Natural Science Foundation of China (32571402) to Y.H., the Distinguished Young Scholars of Hubei Province (2025AFA112) to Y.H., the National Key Research and Development Program of China (2024YFA0917800) to S.W., the Distinguished Young Scholars of Hubei Province (2022CFA078) to S.W., and the Knowledge Innovation Program of Wuhan-Shugung Project (2023020201020418) to S.W.

Author contributions: R.Z., C.J., and Y.H. designed the research. R.Z. prepared the samples, performed the NMR, smFRET and fluorescence experiments, collected the cryo-EM data, performed the AF3 predictions and MD simulations, and analyzed the data. J.W. calculated the cryo-EM structures. X.H. prepared the mutant constructs. X.N. assisted with ^{19}F CEST data collection. C.J. provided supervision on NMR experiments and processing. S.W. provided supervision on cryo-EM data analysis and structure determination. Y.H. provided overall project supervision. R.Z. and

Y.H. provided interpretations of the data, and wrote the manuscript with contributions from all authors.

Competing interests: The authors declare no competing interests.

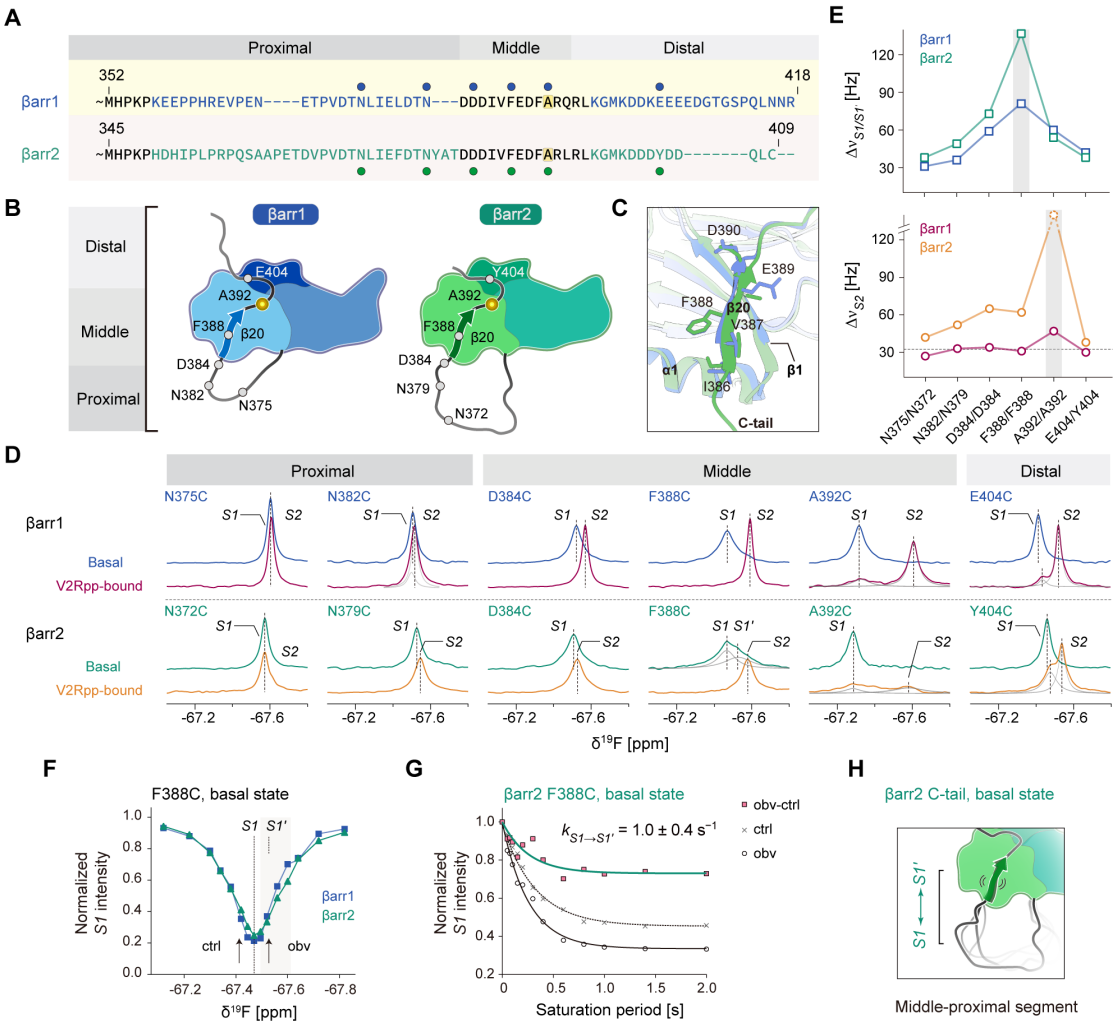

Fig. 1. ^{19}F NMR reveals distinct C-tail dynamics in βarr1 and βarr2. (**A**) Sequence differences in the C-tails of human βarr1 and βarr2. ^{19}F-labeling sites are indicated by filled circles, and the A392 site is highlighted. (**B**) Schematic illustration of the βarr structures showing the locations of the ^{19}F labeling sites, and the spatial dissection of the proximal, middle and distal segments. (**C**) Structural details of the C-tail interaction with the N domain in the basal state of human βarr1 (blue; PDB 8AS4) and rat βarr2 (green; PDB 8J9K). Residues in the β20 segment are shown in sticks. (**D**) ^{19}F NMR spectra of βarr1 (top) and βarr2 (bottom) in the basal and V2Rpp-bound states labeled in different C-tail segments. Gray lines denote deconvoluted peaks. (**E**) Linewidths (Δν) of the ^{19}F NMR resonances in the basal (top) and V2Rpp-bound (bottom) states. The linewidth of βarr2 A392C resonance (*S2* peak) in the V2Rpp-bound state is beyond accurate measurement and is shown as a dashed circle. (**F–G**) ^{19}F CEST profiles of the F388C site in both βarrs in the basal state (F), and the fitting of the $k_{S1–S1'}$ transition rate for βarr2 based on saturation transfer difference experiment (G). In the control experiment (*ctrl*, crossed symbols), the irradiation field was applied at an offset of $\Delta\delta_{S1–S1'}$ from *S1*. The $k_{S1–S1'}$ value was obtained by fitting to a two-state model. (**H**) Schematic model of C-tail dynamics in basal-state βarr2.

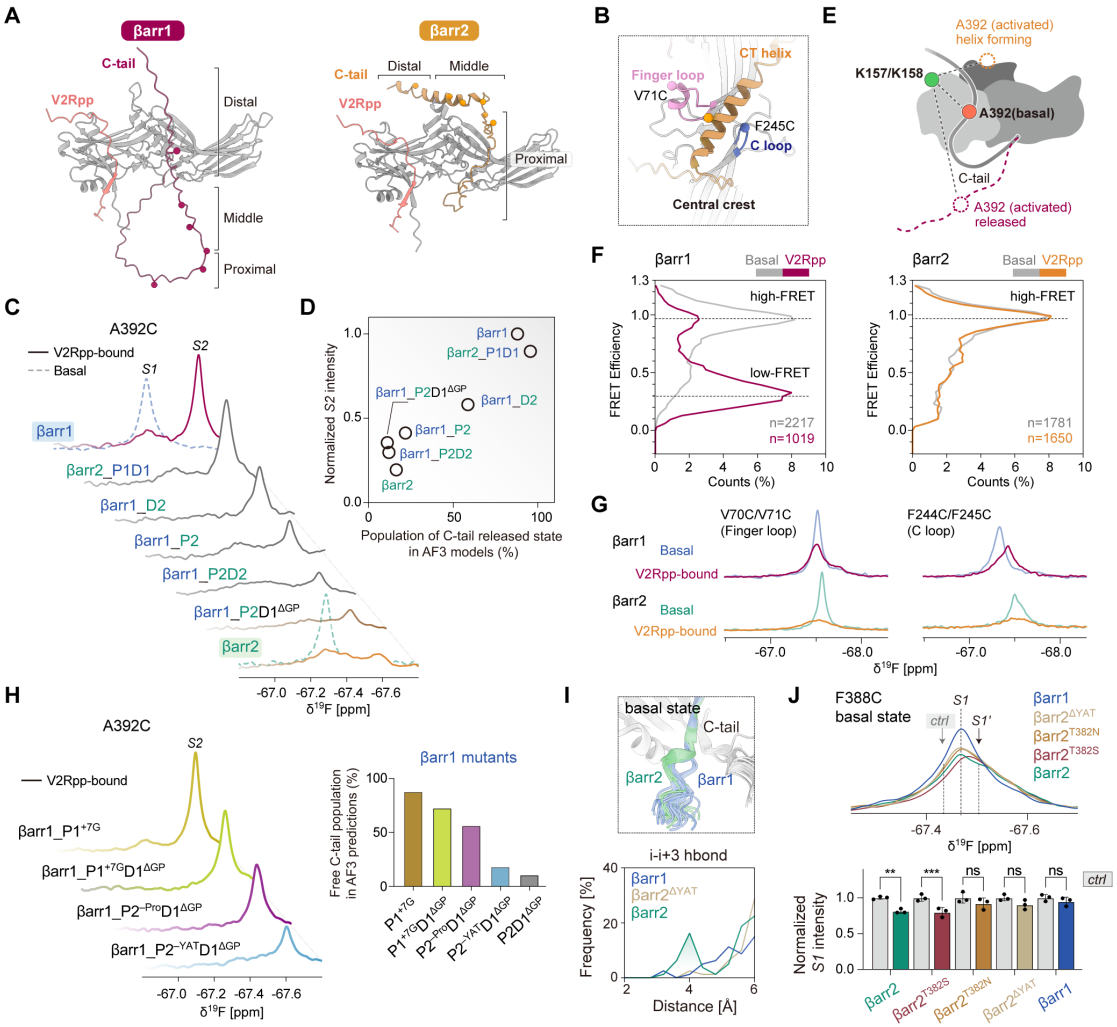

Fig. 2. Molecular basis of helix formation in βarr C-tail. (**A**) Representative AF3 models of V2Rpp-complexed βarr1/2 structures. The C-tail ^{19}F-labeling sites are shown as spheres. (**B**) Local structure in the V2Rpp–βarr2 model showing the binding between the C-tail helix and the central crest. (**C**) ^{19}F NMR spectra of the A392C site in different βarr chimeras in the V2Rpp-bound state (solid lines) compared with native βarr1/2 in the basal (dashed lines) and V2Rpp-bound (solid lines) states. (**D**) Plot of normalized A392C *S2* peak intensities in different βarr chimeras *versus* the population of C-tail released state in AF3 predictions (number of predicted models n_{model} = 92). (**E**) Schematic illustration showing the relative positions of K157/K158–A392 FRET pair in the basal state, and in the activated state with released or helix-forming conformations. (**F**) FRET-efficiency histograms of the K157/K158–A392 pair in the basal and V2Rpp-bound states. (**G**) ^{19}F NMR spectra of the V70C/V71C (finger loop) and F244C/F245C (C loop) sites in βarr1/2 in the basal and V2Rpp-bound states. (**H**) ^{19}F NMR spectra of the A392C site in βarr1 variants with altered C-tail sequence features in the V2Rpp-bound state (left), and the populations of the C-tail released state in AF3 predictions for these variants (right). (**I**) AF3 models of full-length βarrs in the basal state (20 models each), showing local conformation at the junction between the proximal segment and the β20 strand (top), and the frequency of i–i+3 (the i+3 position corresponds to D385) side-chain hydrogen-bond formation in AF3 models for βarr1/2 and the βarr2$^{\Delta YAT}$ mutant (bottom). (**J**) Overlay of the basal-state F388C ^{19}F NMR spectra among βarrs variants with

mutations in the YAT motif (top), and the normalized *S1* peak intensities in a ^{19}F saturation transfer experiment (bottom). The irradiation field was applied either at the *S1'* peak position or at the control frequency with an offset of $\Delta\delta_{S1-S1'}$ from *S1* (*ctrl*). Data are presented as mean values ± SD of n = 3 technical replicates. One-way ANOVA: not significant (ns), $P > 0.05$; $^{*}P < 0.05$; $^{**}P < 0.01$; $^{***}P < 0.001$; $^{****}P < 0.0001$.

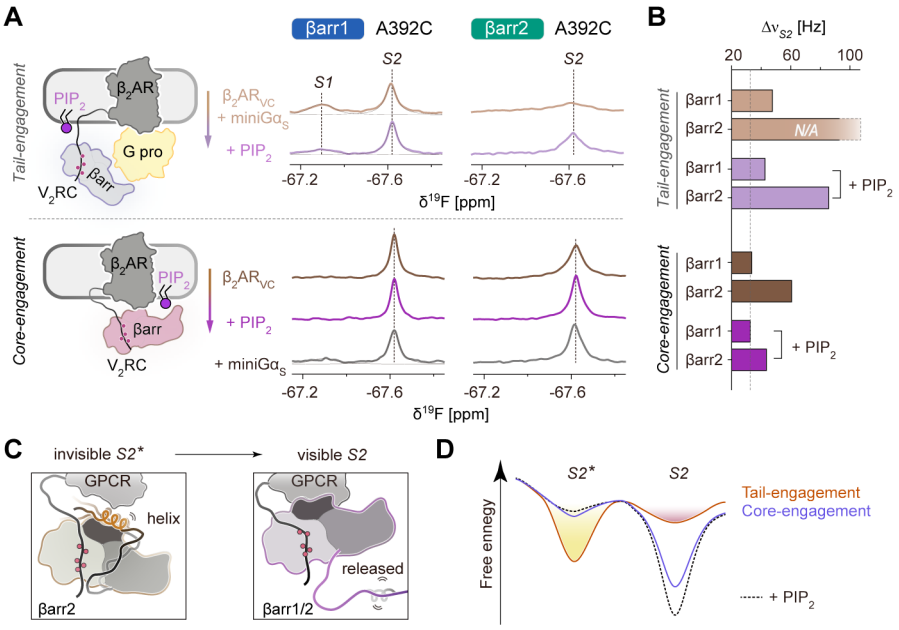

Fig. 3. Transition from tail- to core-engaged state monitored by ^{19}F NMR titration. (**A**) A392C ^{19}F NMR spectra of both βarrs observed under tail- and core-engaged conditions with nanodisc-embedded pβ2ARVC. The arrows indicate sequential additions of different components into the ^{19}F-labeled βarr samples. To prepare the tail-engaged sample, the receptor was pre-incubated with miniGαs before titration with βarrs. (**B**) Linewidth analysis of the A392C *S2* peaks under different conditions shown in panel A. The βarr2 A392C linewidth in the tail-engaged sample without PIP2 is illustrated schematically due to severe broadening. (**C**) Schematic representation of the transition between an NMR-invisible *S2** state (helical) and an NMR-visible *S2* state (released) of βarr2 C-tail. (**D**) An illustrative diagram showing the conformational energy landscapes of βarr2 C-tail in the tail- and core-engaged states. Dashed line indicates PIP2-induced changes of the core-engaged state.

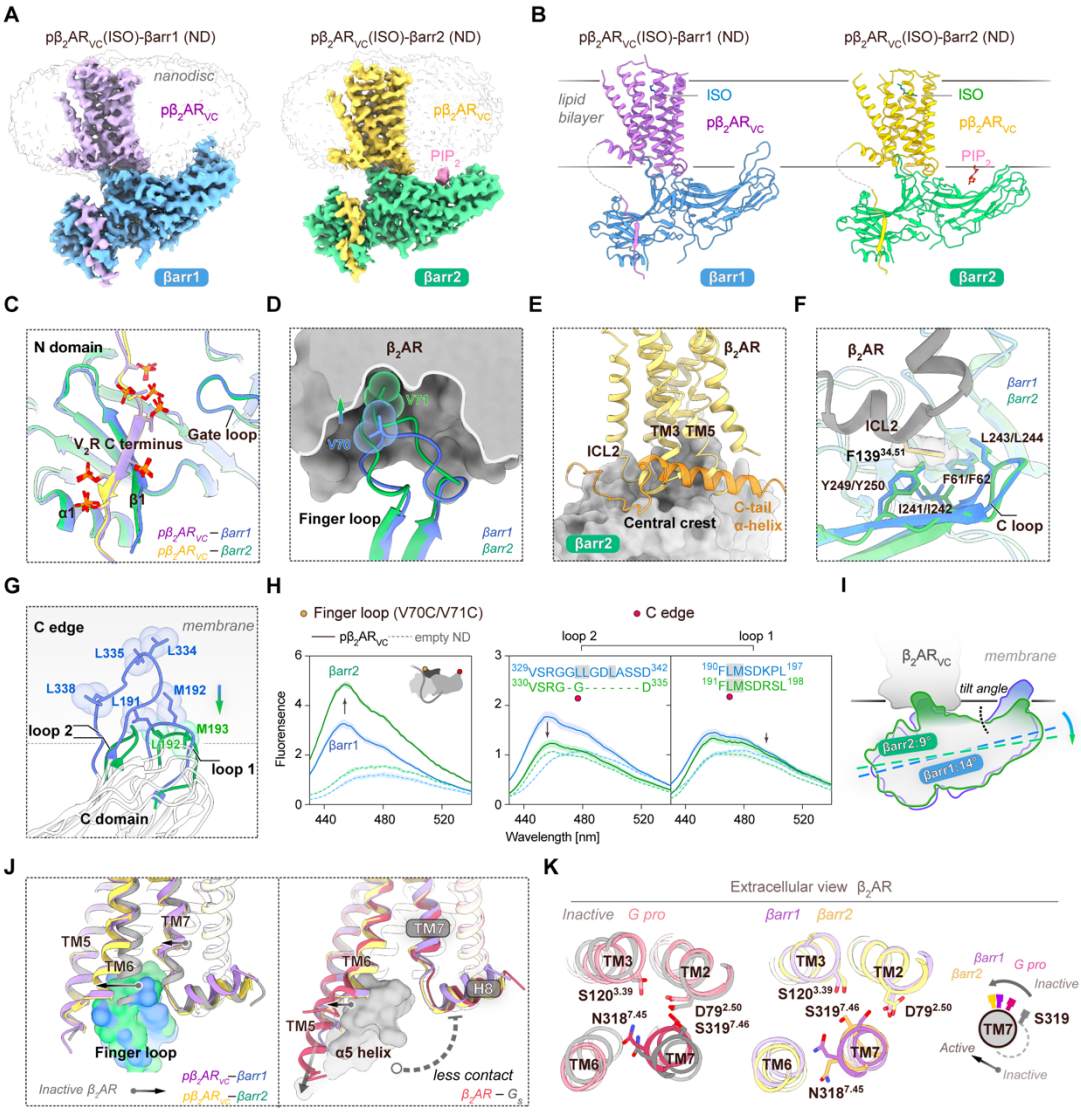

Fig. 4. Cryo-EM structures of the core-engaged pβ2ARVC–βarr1 and pβ2ARVC–βarr2 complexes. (**A**) Cryo-EM maps of the pβ2ARVC–βarr1 (left) and pβ2ARVC–βarr2 (right) complexes reconstituted in nanodiscs. Fab30 and Nb32 used to stabilize the complexes are omitted for clarity. (**B**) Atomic models of the pβ2ARVC–βarr1 (left) and pβ2ARVC–βarr2 (right) complexes. The nanodisc boundary is depicted as a lipid bilayer. (**C**) Local structure of the receptor tail-binding site in βarr N domain showing the resolved phosphate groups in both complexes. (**D**) Local structure of the finger loop–TM core interface showing the different insertion depths between the two complexes. (**E**) Overlay of the pβ2ARVC–βarr2 complex structure with the AF3-predicted structure model of V2Rpp-bound βarr2 harboring a C-tail α-helix. The βarr2 central crest is shown in surface representation (gray). The β2AR TM core (yellow) and the βarr2 C-tail α-helix (orange) are both shown in cartoon representations. (**F**) Binding interface between β2AR ICL2 (gray) and βarr central crest, showing the insertion of $F139^{34.51}$ into a hydrophobic pocket formed by the C loop and finger loop. (**G**) C-edge loop interactions with membrane the pβ2ARVC–βarr1 (blue) and pβ2ARVC–βarr2 (green) complexes. Hydrophobic side chains are shown as sticks. (**H**) mBBr fluorescence measurements at the finger loop (left) and C-edge loops (right) for βarr1 and βarr2 (n = 6

measurements from 3 independent experiments with 2 technical replicates each; shading, ± SD). A schematic illustration showing the two labeling regions is shown as an inset in the left panel. Sequence alignments for the C-edge loops are shown in the right panel with hydrophobic residues shaded gray. Dashed lines correspond to inactive βarr1 and βarr2 measured in the presence of empty nanodiscs (empty ND), and solid lines correspond to βarr1 and βarr2 measured in the presence of nanodisc-embedded $p\beta_2AR_{VC}$. (**I**) A schematic illustration showing different tilt angles of βarr1 and βarr2 relative to the membrane. The tilt angle is calculated using the Cα–Cα vector between F149/F150 and L327/L328 in βarr1/βarr2 (dashed line) as a reference axis relative to the membrane plane. (**J**) Comparison of β_2AR TM conformation changes in the βarr-bound (left) versus G-protein-bound (PDB 3SN6; right) states, with the βarr finger loop and Gs α5 helix shown as surface representations. (**K**) β_2AR TM7 conformational differences between the G-protein-bound and βarr-bound states viewed from the extracellular side, with a schematic illustration highlighting a more pronounced counterclockwise rotation of TM7 in the βarr-coupled states.

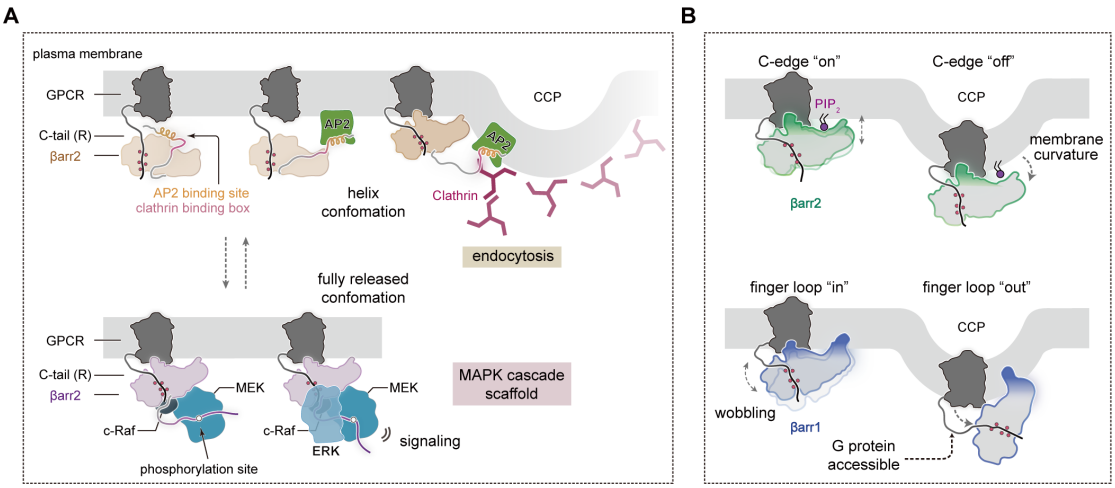

Fig. 5. Conceptual models for isoform-specific GPCR-βarr engagements. (**A**) A hypothesized illustration showing the unique C-tail conformational equilibrium between the tail- and core-engaged states of βarr2 and their potential functional implications. (**B**) A schematic illustration showing the different binding dynamics with lipid membrane in the GPCR-βarr1/2 core-engaged complexes.